analysis, The 15th Auditory Research Forum, Kyoto, Japan, December 4-5 (2010)

49. 藤原 康弘, Fei Zhao, 小池 卓二：有限要素法によるヒト外耳・中耳結合モデルの構築, 日本機械学会 2010 年度年次大会学術講演会 (2010.9)
50. 坂下 輔, 坂本 智明, 小池 卓二：内耳の振動挙動シミュレーション：人工内耳装用方法の最適化, 第2回マイクロ・ナノシンポジウム(2010.10)
51. 藤井 麻起子, 小池 卓二, 神崎 晶：耳硬化症患者における耳小骨可動性計測, 第 2 回マイクロ・ナノシンポジウム (2010.10)
52. 藤井麻起子, 小池卓二, 神崎晶：耳小骨可動性計測装置の開発:圧電材料を用いた力センサの開発, 第 23 回バイオエンジニアリング講演会(2011.1)
53. 坂下 輔, 坂本智明, 小池卓二：外有毛細胞の activity を考慮した蝸牛の振動挙動シミュレーション, 第 23 回バイオエンジニアリング講演会(2011.1)
54. 横井大介, Isaac Juarez Acosta, 小池卓二：蝸牛内基底板の過渡応答シミュレーション, 第 23 回バイオエンジニアリング講演会(2011.1)

G. 知的所有権の取得状況

1) 特許取得

3 件申請検討中

2) 実用新案登録

なし

3) その他

なし

厚生労働科学研究費補助金（障害者対策総合研究事業（感覚器障害分野））
分担研究報告書

MEMS/NEMS 技術を用いた人工感覚上皮の開発に関する研究

研究分担者	川野　聡恭	大阪大学基礎工学研究科
研究分担者	土井　謙太郎	大阪大学基礎工学研究科
研究分担者	新宅　博文	大阪大学基礎工学研究科
研究分担者	舘野　高	大阪大学基礎工学研究科

研究要旨：　本研究では，蝸牛の機能を代替する人工感覚上皮を開発し，新しい人工聴覚システムを確立することを目的としている．本年度は，これまでに開発した人工感覚上皮を発展させ，薄膜化による出力の増大を目指した．その結果，従来比約 20 倍の起電力を得ることができた．また，周波数弁別能の広帯域化を目的として，膜厚の異なる振動体アレイを大量に製造する微細加工プロセス技術を開発した．そして，膜厚変化の効果により，試作した振動体アレイの周波数帯域が約 8 倍に増大していることを明らかにした．

A.　研究目的

本研究では，蝸牛の機能を代替する人工感覚上皮を MEMS/NEMS (Micro / Nanoelectromechanical systems)技術により開発し，体外機器を要しない人工聴覚システムの確立を目指している．分担者らはこれまでに，周波数弁別能を有する圧電センサ，すわなち，人工感覚上皮の開発およびそれを用いたモルモットでの聴性脳幹反応記録に成功している．これらの成果を基盤として，本研究では臨床的な有効性が期待できる人工感覚上皮を創成する．

本年度は，これまでに製作した人工感覚上皮の起電力増加および周波数弁別能の広帯域化を目的とした新しい加工プロセスを開発した．以下にそれぞれの項目に関する研究の進捗状況を記す．

B.　薄膜化技術による人工感覚上皮の起電力増加

人工感覚上皮は圧電材料を主な構成要素としており，音波の入力により曲げ振動を生じ，圧電効果により電気信号を出力する．圧電膜の外形を細長い台形状としたため，局所的な特徴周波数（幅方向の共振周波数）が連続的に変化する．また，人工感覚上皮表面には，微小電極アレイが配置されており，各電極からの電気的な出力は各部の振動特性に依存する．すなわち，電気信号はその位置における局所的な特徴周波数において増大する．この特性により，人工感覚上皮は生体の内耳が有する周波数弁別能を人工的に再現できる．一方，簡単な試算から，人工感覚上皮の電気的出力は，膜厚に反比例することが理論的に示される．そこで，本研究では，薄膜化技術により人工感覚上皮の振動特性を向上し，起電力を増加することを目指した．

人工感覚上皮の加工プロセスを以下に示す．まず，スパッタリング法によりSOI (Silicon On Insulator)基板上に厚さ40 nmのTi薄膜および厚さ460 nmのPt薄膜を成長させ，下部電極を形成した．次にPt表面に厚さ400 nmのポリフッ化ビニリデン三フッ化エチレン共重合体(P(VDF-TrFE))をスピンコーティング法により形成した．その後，結晶化のために145 ℃で6時間加熱した．そして，シャドウマスクを用いた熱蒸着法により，P(VDF-TrFE)表面に上部電極を形成した．上部電極は人工感覚上皮の境界上に配置してある．これは，境界において，ひずみが

最大になることを利用して，比較的大きな電気的出力を得るためである．さらに，Deep RIE (Deep Reactive Ion Etching)を用いて，SOI基板の裏側からSiをエッチング加工し，台形状の振動膜を作製した．膜の形状は全長が30 mmであり，幅は0.3 mmから2.8 mmまで線形的に変化する．最後に，上部および下部電極間に電圧を加え，P(VDF-TrFE)を分極処理した．

製作した人工感覚上皮の特性は，音の入力に対する出力電圧を計測することで調べた．まず，印可音圧が100 dB一定の条件で，入力音の周波数を変化させながら出力電圧を計測した．次に，出力電圧の振幅が最大になる周波数をその電極位置における特徴周波数と定義し，その周波数に固定した条件で，出力電圧を計測した．印可音圧を60 dBから100 dBの範囲で変化させて計測したところ，電圧振幅は音圧とともに増加し，100 dBにおいて最大で8.0 mVの信号を出力することが分かった．ここで得られた音圧と出力電圧の関係について，過去の研究において製作した人工感覚上皮と比較すると，薄膜化したそれは約20倍の起電力を有することが分かった．しかしながら，蝸牛管内部に挿入した電極を介した刺激法，すなわち従来の人工内耳と同様の方法では，1 V程度の電圧が必要であり，ここで得られた出力電圧で十分に聴覚神経を刺激できないと考えられる．そのため，今後，更なる起電力増加，電圧増幅法の開発および電極の改良による刺激効率の向上等が必要であると考えられる．

C. 広帯域周波数弁別能を実現する人工感覚上皮の開発

これまで開発した人工感覚上皮では，膜幅を調整することで，局所的な特徴周波数の変化を実現した．これは，製作に用いている微細加工技術が，基本的に2次元構造を製作する技術であり，これを用いた3次元構造の製作が困難であることに起因する．一方で，膜の厚みが一定であるために，人工感覚上皮の応答する周波数帯域は1 - 5 kHz程度であり，人の可聴域(20 Hzから20 kHz)よりも狭いという課題があった．生体の基底膜が幅のみならず厚みの変化により，幅広い周波数帯への応答を可能としていることからも，人工感覚上皮を製作する上で厚み変化の付与が重要であると考えられる．

そこで，本研究では，人工感覚上皮の周波数帯域拡大を目的とし，幅および厚みが連続的に変化する振動体を大量かつ簡便に製作する方法を考案し，新たに振動梁の集合体で構成される人工感覚上皮を開発した．人工感覚上皮の厚みを制御するために，ここではグレイスケールリソグラフィとネガ型フォトレジストを用いた方法を考案した．ネガ型フォトレジストは，紫外光が照射された領域が現像液に対して不溶化する材料である．フォトレジスト表面から露光を行った場合，通常，表面付近のフォトレジストが多くのエネルギを吸収し，内部の領域ほどその吸収量は少なくなる．そのため，フォトレジスト全体の厚みに対して不十分なエネルギ量で露光すると，フォトレジスト表面が現像液に対して不溶性となる一方で，内部，特に基板近傍のフォトレジストは，現像液に溶解する状態で残る．さらに，グレイスケール，すなわち光透過性が0-100 %の間で制御されたパターンを介してネガ型フォトレジストを露光した場合，不溶化するフォトレジストの厚み制御が可能である．この原理を利用して，ネガ型フォトレジストを露光し，現像することで，基板上に厚みの異なる振動体構造とその支持構造を同時に製作することが可能である．

本方法の有効性を示すために，光透過性が20 - 50 %の間で連続的に変化するフォトマスクを製作し，ネガ型レジストSU-8 3050を用いて微小振動梁の集合体から成る振動体アレイを試作した．振動体アレイは全長20 mmの領域に両端固定の振動梁を64 本有し，各梁の長さは，1 mmから2 mmまで線形的に変化する．試作の結果，振動梁の厚みを6.6 ～49 μmの範囲で変化させることに成功した．さらに，製作した振動梁の周波数特性をレーザドップラ振動計により計測した．ここでは，振動梁からの反射光を十分に得るために，振動測定に先立って振動梁表面に約50 nmのAl薄膜を形成した．ただし，振動梁と比較してAl薄膜が十分に薄いことからAl薄膜が振動特性に及ぼす影響は無視できると考えられる．膜厚変化のない振動体アレイの場合，13.8 kHz - 49.0 kHzの範囲の共振周波数を有する一方，膜厚変化のある振動体アレイの場合，16.7 kHzから502 kHzの範囲の共振周波数を有することが分かった．以上の結果から，厚み変化により約8倍の広帯域化に成功したことが分かる．なお，本計測は空気中における共振周波数を測定したものであり，実際の駆動条件であるリンパ液中では，周囲流体の影響により共振

周波数は可聴域付近にまで減少することが見込まれる．今後は，液体中における振動特性について検討し，さらに知見を深めたいと考えている．

D. 研究発表

1. 論文発表

(1) Hirofumi SHINTAKU, Takashi TATENO, Nobuyoshi TSUCHIOKA, Harto TANUJAYA, Takayuki NAKAGAWA, Juichi ITO, and Satoyuki KAWANO, Culturing Neurons on MEMS Fabricated P(VDF-TrFE) Films for Implantable Artificial Cochlea, Journal of Biomechanical Science and Engineering, Vol.5, No. 3 (2010), pp. 229-235.

(2) T. Tateno, The hyperpolarization-activated current regulates synchronization of gap-junction coupled dopaminergic neurons in the midbrain, IEEJ Transactions on Electrical and Electronic Engineering (in press).

(3) T. Tateno, Morphological properties in dopaminergic neurons of the rat midbrain during early developmental stages and one numerical approach to passive-membrane modeling, IEE Japan Transactions on Electronics, Information and Systems, Vol. 131, No. 1, Sec. C, 50-55 (2011).

(4) N.W. Gouwens, H. Zeberg, K. Tsumoto, T. Tateno, K. Aihara, and H.P.C. Robinson, Synchronization of firing in cortical fast-spiking interneurons at gamma frequencies: a phase-resetting analysis, PLoS Computational Biology, 6 (9): 1-13 (2010).

(5) T. Tateno, A small-conductance Ca^{2+}-dependent K+ current regulates dopamine neuron activity: a combined approach of dynamic current clamping and intracellular imaging of calcium signals, NeuroReport 21 (10): 667-674 (2010).

2. 学会発表

(1) Hirofumi SHINTAKU, Takatoshi INAOKA, Yohei NAKAMOTO, Masahide HAYASHI, Yoichi KAGAYA, Takayuki NAKAGAYA, Juichi ITO, and Satoyuki KAWANO, Measurement of Electrically Evoked Auditory Brainstem Response Using Bionic Auditory Membrane with Frequency Selectivity, Technical Digest of the 5th Asia-Pacific Conference on Transducers and Micro-Nano Technology, Perth, Australia, July (2010), p.90.

(2) Masahide HAYASHI, Hirofumi SHINTAKU and Satoyuki KAWANO, Development of Bionic Auditory Membrane Equipped with Electrical Circuits for Stimulating Cochlear Ganglion Cells, Proceedings of Seventh International Conference on Flow Dynamics, Sendai, Japan, November (2010), pp. 654-655.

(3) Hirofumi SHINTAKU, Satoyuki KAWANO, Takayuki NAKAGAWA, and Juichi ITO, Vibration Dynamics of Bionic Auditory Membrane for a Novel Artificial Cochlea, Proceedings of Sixth International Symposium on Meniere's Disease and Inner Ear Disorders, Kyoto, Japan, November (2010), p. 207.

(4) Yobuyosi TSUCHIOKA, Hirofumi SHINTAKU, Takashi TATENO, Satoyuki KAWANO, Takayuki NAKAGAWA, and Juichi ITO, Recording Evoked Activity of Neocortical Neurons on Multi-Electrode-Array Substrates in Response to Output Signals from Bionic Auditory Membrane, Proceedings of Sixth International Symposium on Meniere's Disease and Inner Ear Disorders, Kyoto, Japan, November (2010), p. 208.

(5) Toshiya KANBE, Hirofumi SHINTAKU, Satoyuki KAWANO, Takayuki Nakagawa, Juichi ITO, Development of Bionic Auditory Membrane for Implantation into Cochleae of Guinea Pigs, Proceedings of Sixth International Symposium on Meniere's Disease and Inner Ear Disorders, Kyoto, Japan, November (2010), p. 208.

(6) 新宅博文，川野聡恭，人工内耳用 MEMS 音響センサの振動特性とそのモデル化，日本機械学会 2010 年度年次大会講演論文集(8), pp. 125-126, 名古屋，2010 年 9 月.

(7) 神戸俊也，新宅博文，川野聡恭，時間変動音を用いた多電極の MEMS 人工内耳の応答計測，日本機械学会第 23 回バイオエンジニアリング講演会講演論文集，p. 247, 熊本，2011 年 1 月.

(8) 土岡伸嘉，新宅博文，川野聡恭，神経回路網への局所物質導入を可能とする微小流路ネットワーク，日本機械学会第 23 回バイオエンジニアリング講演会講演論文集，p. 391,熊本，2011 年 1 月.

研究成果の刊行に関する一覧表

著書

なし

論文

発表者氏名	論文タイトル名	発表雑誌名	出版年・巻号・頁
Tateno T.	The hyperpolarization-activated current regulates synchronization of gap-junction coupled dopaminergic neurons in the midbrain.	IEEJ Transactions on Electrical and Electronic Engineering	in press
Tateno, T.	Morphological properties in dopaminergic neurons of the rat midbrain during early developmental stages and one numerical approach to passive-membrane modeling.	IEE Japan Transactions on Electronics, Information and Systems	2011. 131, No. 1, Sec. C, 50-55.
N.W. Gouwens, H. Zeberg, K. Tsumoto, T. Tateno, K. Aihara, and H.P.C. Robinson.	Synchronization of firing in cortical fast-spiking interneurons at gamma frequencies: a phase-resetting analysis.	PLoS Computational Biology	2011. 6 (9): 1-13.
Tateno T.	A small-conductance Ca2+-dependent K+ current regulates dopamine neuron activity: a combined approach of dynamic current clamping and intracellular imaging of calcium signals.	NeuroReport	2010. 21 (10): 667-674.
Shintaku H, Nakagawa T, Kitagawa D, Tanujaya H, Kawano S, Ito J..	Development of piezoelectric acoustic sensor with frequency selectivity for artificial cochlea.	Sensors and Actuators, A: Physical.	2010;158(2):183-192.
Shintaku H, Tateno T, Tsuchioka N, Tanujaya H, Nakagawa T, Ito J, Kawano S..	Culturing neurons on MEMS fabricated P(VDF-TrFE) films for implantable artificial cochlea..	Journal of Biomechanical Science and Engineering	2010;5(3):229-235.

Ogita H, Nakagawa T, Sakamoto T, Inaoka T, Ito J..	Transplantation of bone marrow-derived neurospheres into guinea pig cochlea..	Laryngoscope.	2010;120(3):576-581.
Sakamoto T, Nakagawa T, Horie RT, Hiraumi H, Yamamoto N, Kikkawa YS, Ito J.	Inner ear drug delivery system from the clinical point of view.	Acta Otolaryngol Suppl.	2010(563):101-104.
Hiraumi H, Yamamoto N, Sakamoto T, Ito J.	Cochlear implantation in patients with prelingual hearing loss.	Acta Otolaryngol Suppl.	2010(563):4-10.
Hiraumi H, Yamamoto N, Sakamoto T, Ito J.	Multivariate analysis of hearing outcomes in patients with idiopathic sudden sensorineural hearing loss.	Acta Otolaryngol Suppl.	2010(563):24-28.
Sekiya T, Matsumoto M, Kojima K, Ono K, Kikkawa YS, Kada S, Ogita H, Horie RT, Viola A, Holley MC, Ito J.	Mechanical stress-induced reactive gliosis in the auditory nerve and cochlear nucleus.	J Neurosurg.	2010. DOI:10.3171/2010.2.JNS091817, Apr 2
Ishihara K, Okuyama S, Kumano S, Iida K, Hamana H, Murakoshi M, Kobayashi T, Usami S, Ikeda K, Haga Y, Tsumoto K, Nakamura H, Hirasawa N, Wada H.	Salicylate restores transport function and anion exchanger activity of missense pendrin mutations.	Hear Res.	2010. 270:110-118
Kumano S, Murakoshi M, Iida K, Hamana H, Wada H.	Atomic force microscopy imaging of the structure of the motor protein prestin reconstituted into an artificial lipid bilayer.	FEBS Lett	2010. 584:2872-2876

Kumano S, Iida K, Ishihara K, Murakoshi M, Tsumoto K, Ikeda K, Kumagai I, Kobayashi T, Wada H.	Salicylate-induced translocation of prestin having mutation in the GTSRH sequence to the plasma membrane.	FEBS Lett	2010. 584:2327-2332

Paper

The hyperpolarization-activated current regulates synchronization of gap-junction coupled dopaminergic neurons in the midbrain

— A combined approach between computational modeling and electrophysiological recording —

Takashi Tateno*, **, Member

To examine the functional role of hyperpolarization-activated and cyclic nucleotide-gated (HCN) current observed in mesencephalic dopaminergic neurons, we constructed a conductance-based model that can mimic the electrical properties obtained in electrophysiological recordings of rat brain slices. In the model, blocking the HCN current resulted in a reduction of spontaneous firing rate and a change in the properties of autonomous pacemaking. In addition, reduced one-dimensional phase equations and their coupled oscillators were analyzed. The analysis indicated that HCN channels can regulate the extent of synchronization of coupled dopaminergic neurons through gap-junction connections. Thus, the HCN current can effectively shape the autonomous and cooperative firing of dopaminergic neurons in the midbrain.

Keywords : conductance-based model, coupled oscillators, electrophysiological recording, phase equation, stability analysis

1. Introduction

Mesencephalic dopaminergic (DA) neurons play a key role in the functions of the basal ganglia including reward-based learning [1], cognition [2], and motor control [3]. Although recent studies have provided significant insights into the properties of many ion channels expressed in DA neurons [4], little attention has been paid to hyperpolarization-activated and cyclic nucleotide-gated (HCN) channels and their roles in neural information processing. Among vertebrate voltage-gated ion channels, HCN channels have two unique properties: (i) they have a reverse voltage dependence that leads to activation upon hyperpolarization; and (ii) voltage-dependent opening of these channels is directly regulated by the binding of cyclic adenosine monophosphate (cAMP) [5]. However, a direct link between HCN channels and superthreshold membrane-voltage phenomena such as firing rate modulation and the synchronization of action potentials among DA cells has not been systematically investigated.

In this study, to understand the functional role of HCN channels systematically, we first constructed a conductance-based Hodgkin–Huxley type DA cell model on the basis of reported results in the literature and data recoded from DA cells in rat midbrain slices. Second, to gain some insight into synchronized phenomena in gap junction-coupled DA neurons, a weak coupled-oscillator phase-equation model of two identical DA neuron pairs was derived after numerically computing the phase resetting curves of regular firing using the conductance-based model. Third, to examine synchronized phenomena among DA cells, a stability analysis of synchronization between coupled oscillators was applied to the model. The results indicated that HCN channels can regulate not only the frequency of firing and subthreshold oscillations in membrane voltage but also the extent of synchronization and desynchronization among DA cells. Hence, the study presented here shed light on to a new functional role in DA cells of the midbrain, using computational and electrophysiological approaches.

* PRESTO, Japan Science and Technology Agency, 4-1-8 Honcho, Kawaguchi, Saitama, Japan
** Graduate School of Engineering Science, Osaka University, 1-3, Machikaneyama, Toyonaka, Osaka, 560-8531 Japan

2. Materials and methods

2.1 Electrophysiological recording

At a temperature of 34°C, we recorded membrane voltage from DA neurons in slices of rat midbrain from animals aged 14–16 days. For details of the preparation, solutions, and whole-cell recording technique, see Ref. [6]. All procedures in this study were approved by Osaka University and complied with the NIH Guidelines for Animal Use.

2.2 A conductance-based model

First, the somatic and single-compartment model was represented by the following equations according to the Hodgkin–Huxley type conductance-based scheme [7]. The model includes ion channel currents that are known to exist in the somata of DA cells. The model is based on those reported by Amini et al. [8] and Kuznetsov et al. [9]. However, some terms in the current balance equation such as ATP-pump and Na^+/Ca^{2+}-exchanger mechanisms were omitted for simplicity. Instead, several ion channel current terms were added on the basis of some recent electrophysiological studies described below. In addition, some parameters in the models were modified from data in the recent literature and from the recording carried out in the present study. The current balance equation in a soma is described by

$$C_m \frac{dV}{dt} = -(I_{Na} + I_K + I_A + I_M + I_h + I_{Ca} + I_{SK} + I_L) + I_{app} \quad \cdots\cdots (1)$$

where C_m is the somatic membrane capacitance and V is the somatic membrane potential. The above model includes the transient Na^+ current (I_{Na}), delayed rectifier K^+ current (I_K), A-type K^+ current (I_A), muscarinic-sensitive K^+ current (I_M), hyper-polarization activation current (I_h), leakage current (I_L), Ca^{2+} current (I_{Ca}), Ca^{2+}-activated K^+ or SK current (I_{SK}), and an externally applied current (I_{app}). Furthermore, the Ca^{2+} current has the following four subtypes:

$$I_{Ca} = I_{CaL} + I_{CaN} + I_{CaP} + I_{CaT} \quad \cdots\cdots (2)$$

where I_{CaL}, I_{CaN}, I_{CaP} and I_{CaT} represent L-type, N-type, P-type, and T-type Ca^{2+} currents, respectively, and they are different in their voltage dependency.

Excluding I_{SK}, for an ion channel type j, the current description (I_j) can be written by

$$I_j = g_j m_j^{a_j} n_j^{b_j} (V - E_j) \quad \cdots\cdots (3)$$

where g_j, m_j, n_j and E_j are a maximum conductance, the Hodgkin–Huxley type activation and inactivation gating variables, and the reversal potential of the ion, respectively. Here, a_i and b_j are some non-negative integers. The gating variables are solutions of the following first-order differential equation described by

$$\frac{dz}{dt} = \frac{z_\infty(V) - z}{\tau_z(V)} \quad \cdots\cdots (4)$$

where z is one of the gate variables (i.e., m_j or n_j). In Eq. (4), $z_\infty(V)$ and $\tau_z(V)$ are the voltage-dependent steady-state value and time-constant of the gating variable z at membrane voltage V, respectively.

For simplicity, we characterized the steady-state variable by a sigmoid or Boltzmann-type relationship, and the time constant (in ms) by a Gaussian relationship; they are described in the Appendix. Individual ionic membrane currents were characterized by their fit to published voltage-clamp experimental data, which are available in the literature, or to unpublished data recorded in our experiment. In addition, we used some ion-channel kinetics models from published DA neuron models [8,9]. However, data fitting obtained from voltage-clamp recording is not the only criteria for formulating ionic current descriptions. These descriptions may have to be modified to fit whole-cell membrane potential data in our experiments. These adjustments are justified considering that the voltage-clamp experiments were performed on a particular DA cell of a particular mouse, for example, and there is considerable variation in the waveform of the ionic current response from cell to cell. Therefore, we adjusted the model parameters (specifically, several maximum conductance values of ion channels) to fit the data in our experiment.

Calcium dynamics of the soma is described as

$$\frac{d[Ca^{2+}]_i}{dt} = \frac{2\beta}{\tau z_{Ca} F}\left(-I_{Ca} - z_{Ca} F P_{Ca} [Ca^{2+}]_i\right) \quad \cdots\cdots (5)$$

where $[Ca^{2+}]_i$ is the intracellular Ca^{2+} concentration of the soma and I_{Ca} is the sum of all the calcium currents. Intracellular Ca^{2+} was removed from the cell by an unsaturable pump with maximum rate density P_{Ca}, and the pump was treated as nonelectrogenic. β is the ratio of free to total calcium, τ is the time constant of $[Ca^{2+}]_i$ changes, z_{Ca} is the valence of calcium, and F is Faraday's constant.

2.3 Model parameter selection

In the following section, we describe the kinetics of the ion channels in the above model and parameters in detail. The voltage-dependent activation and/or inactivation curves and time constant used in the model are given in Appendix.

Transient Na^+ current (I_{Na}) and delayed rectifier K^+ current (I_K). The I_{Na} and I_K gating kinetics are the same as those written in Kuznetsov et al. [9]. For The I_{Na} and I_K gating kinetics in the model, the order pairs (a_j, b_j) of the activation and inactivation variables in Eq. (3) are (3, 1) and (4, 0), respectively. However, the voltage-dependency functions of the gate variables and time constants are mimicked by using a sigmoid relationship and by a Gaussian relationship, respectively, as stated previously. The maximum conductance values g_{Na}=120 mS/cm^2 and g_K=0.2 mS/cm^2 and the reversal potential values E_{Na}=55 mV and E_K=−90 mV were used.

Transient outward A-type potassium current (I_A). The 4-aminopyridine (4-AP)–sensitive, or A-type potassium current (I_A), has been observed in DA neurons [10,11]. The A-type potassium current in DA neurons can contribute to spontaneous firing and plays a role in the regulation of action-potential frequency by slowing the recovery of the membrane potential to baseline levels [10,12]. The steady state activation and inactivation characteristics of I_A were determined by fitting published voltage-clamp data [11]. The order pair of the activation and inactivation variables is (3, 1). The maximum conductance value g_A=0.5 mS/cm^2 was used.

Muscarinic-sensitive K^+ current (I_M). The muscarinic-sensitive K^+ current or M-current (I_M) is a voltage-dependent slow delayed rectifier K^+ current and is activated at the subthreshold range of the membrane potential. This current is also known to be Tetraethylammonium chloride (TEA) sensitive and contributes to the regulation of action potential generation and excitability [13]. I_M has been shown to be present in midbrain DA neurons with intracellular voltage-clamp recording in brain slices [14,15]. The order pair of the activation and inactivation variables is (1, 0). The maximum conductance value g_M=15.0 μS/cm^2 was used.

Hyperpolarization-activated cation current (I_h). Doperminergic neurons have a hyperpolarization-activated cation current (I_h) [16,17]. The voltage dependency of steady state activation of I_h was determined by fitting our unpublished data, which was recorded from rat midbrain slices in our voltage-clamp recording experiments. In the I_h model, the voltage dependency of conductance and time constant are similar to the model in Amini et al. [8], although the parameters were different on the basis of the data [16,17] (see also Appendix A). The order pair of the activation and inactivation variables is (1, 0). The reversal potential E_h=−39.0 mV was used. In this analysis, the maximum conductance value g_h=0.135 mS/cm^2 was used as the default value; however, the value was changed in some analyses described in Results to examine the effects of HCN channel expression.

Calcium currents (I_{Ca}). As described previously, the model includes L-, N-, P-, and T-type voltage-dependent calcium currents. For L-, N-, and P-type calcium currents, the voltage dependency of a steady-state of the gate variables and the time constant functions was obtained after fitting the parameters to conductance–voltage (g–V) relationships reported in Durante et al. [18]. Similarly, for the low-threshold T-type Ca^{2+} current, the voltage dependency of a steady state of the gate variables and time constant functions was obtained from results in Kang and Kitai [19]. Our parameters are modifications of those used by Amini et al. [8] because of our g-V function selection. The reversal potential for the calcium currents has been set to a constant 100 mV as used in Kuznetsov et al. [9] (i.e., E_{Ca}=−100 mV). For the L-, N-, P-, and T-types of calcium current, the order pairs of the activation and inactivation variables were (1, 0) (1, 1), (1, 1), and (1, 1), respectively, and the maximum conductance values g_{CaL}=0.15, g_{CaN}=0.0375, g_{CaP}=0.0375, and g_{CaT}=0.02 in mS/cm^2 were used.

Calcium-activated small-conductance potassium current (I_{SK}). DA neurons are known to contain at least two types of calcium-activated potassium currents [20]. The apamin-sensitive, small-conductance (SK) Ca^{2+}-activated K^+ current or slow afterhyperpolarization (AHP) current is included in the model. The SK channel conductance (g_{SK}) was represented as

$$g_{SK}([Ca]_i) = g_{SK}\frac{[Ca]_i^4}{[Ca]_i^4 + K_m^4} \quad \cdots\cdots (6)$$

The conductance model was the same as that reported in Kohler et al. [21]. The conductance depends on the forth power of intracellular calcium concentration ($[Ca^{2+}]_i$) to best represent the known characteristic of the SK channel [21]. The calcium half-activation concentration value K_m has been set to 250 nM [9,22]. The other Ca^{2+}-dependent K^+ current is the big-conductance (BK) or maxi-type channel, which is known to be apamin-insensitive and blocked by TEA. Although the BK channel current is associated with the modulation of excitability because of its role in producing a fast AHP [20], it is less essential for slow underlying oscillations and super-threshold spiking behaviors than the SK channel current. In the present study, therefore, we have excluded the BK current from our model. The maximum conductance value g_{SK}=50.0 μS/cm^2 was used.

Leak current (I_L). The present model includes a nonspecific linear background current without gate variables. This current is the main component of the input resistance of the model. In current-clamp recording, we measured the input resistance of DA neurons using 600-ms hyperpolarizing current pulses with amplitude −10 to −20 pA by holding the potential at −60 mV, and the average input resistance of DA cells was 630 MΩ. The result showed that the conductance value g_L was 12.0 μS/cm^2 by assuming the soma was a cylinder whose diameter and length were 14 μm and 30 μm, respectively. The reversal potential value was set to E_K=−90 mV as used in Kuznetsov et al. [9]. In the current balance Eq. (1), the somatic membrane capacitance C_m=1 μF/cm^2 was used.

Calcium dynamics. The parameters in Eq. (5) were the same those used in the Kuznetsov et al. model [9]: β=0.050, τ=4.0 ms, z_{Ca}=2.0, and P_{Ca}=2,500 μm/s.

Computer simulations were performed using XPPAUT [23] with the stiff method and Matlab Ver. 7.5 (Mathworks, Natick, Massachusetts, U.S.A.) with a nonstiff solver (a build-in function of the Runge–Kutta 4th/5th-order method, ode45). A time step of 50 μs was used in all computer simulations.

2.4 Phase-resetting curves.

DA neurons *in vivo* and *in vitro* show spontaneous periodic activity at the rate of 0.5–4.0 Hz. Generally speaking, the mechanisms underlying such periodic activity of a system can be complex with many hidden variables, and all dynamical variables in such a system thus cannot be directly observed. However, useful information about the dynamics of the system can be gained by studying phase-resetting curves (PRCs) [24], which describe the phase shift of the oscillation in response to a perturbing pulse of variable amplitude at each phase of the oscillation. A perturbation is weak if its effect on the amplitude and intrinsic period is negligible. This approximation is often valid in firing neurons, where a small current pulse delays or advances the next spike (action potential) without changing its shape or average firing frequency. However, to construct precise PRCs, we need to apply short pulse-like stimulation to neurons repetitively at many phase points during one cycle for a long time [25]. As the experimental method usually damages neurons, it is hard to obtain true PRCs in electrophysiological experiments. In contrast, if we have a complete description of periodic oscillations, and if it is written by a set of ordinary differential equations, the PRC is directly calculated using the adjoint method proposed by Williams and Bowtell [26]. Because such a complete description of dynamical variables is impossible in real neurons, therefore, PRCs obtained from the present model can give a reasonable counterpart in DA neurons.

2.5 A coupled oscillator model and its stability analysis

To gain some insight into synchronized phenomena in gap junction-coupled DA neurons, a weakly coupled one-dimensional phase-equation model of two identical DA neurons was constructed. If the neural oscillators have robust limit cycles, the full equations reduce to ones whose interactions are through the differences in the phases of their periodic cycles. Much has been written about such coupled phase-oscillators (see Koppel and Ermentrout [27] and Hoppensteadt and Izhikevich [28] for review). Here, we assume that two identical neural oscillators are reduced to two phase equations as following: for i, j=1 or 2,

$$d\theta_i / dt = \omega_0 + \varepsilon H(\theta_i - \theta_j) \quad (i \neq j), \quad \cdots\cdots (7)$$

where θ_1 and θ_2 are phases in the two limit cycles, ω_0 is the frequency of the uncoupled oscillators, and ε is a small parameter. The interaction function H is T-periodic in the argument and it can be explicitly computed from the original set of Eqs. (1)–(5). Let $\phi = \theta_2 - \theta_1$. Then,

$$H(\phi) = g / T \cdot \int_0^T P(t)\left[V_0(t+\phi) - V_0(t)\right]dt, \quad \cdots\cdots (8)$$

where g is the conductance of gap-junction coupling between the cells, T is the period of the original limit cycles, $P(t)$ is the PRC, and V_0 (t) is the membrane voltage of the original limit cycles. In Eq. (8), the conductance g only contributes the function H as a scale factor. In the following, therefore, we consider g=1.0 μS/cm^2. The function of $P(t)$ is the normalized T-periodic solution to the adjoint equation of the present model and numerically computed by the method proposed by Williams and Bowtell [26]. One of the goals of the analysis in this study is to determine the stability of the synchronous, phase-locked, and antiphase-locked solutions, and how it depends on the parameters (specifically, the HCN channel conductance) in the model. It is known that a phase-locked solution ϕ_i is stable if and only if $dH(\phi_i)/d\phi > 0$ [29]. In particular, the synchronous phase-locked solution is stable if and only if $dH(0)/d\phi > 0$. In many neural systems, there exists the possibility of delays at many levels. In particular, there are delays due to axonal and dendritic propagation, and delays encountered when gap-junction coupling was far from the source of the oscillation or the spike initiation zone and must be communicated through dendrites. In the simplest case, a delay effect is described by a phase transition of the interaction function with delay τ.

$$H_\tau(\phi) = H(\phi - \tau). \quad \cdots\cdots (9)$$

This relationship is appropriate when there is a delay between $P(t)$ and $V_0(t)$ in Eq. (8) [29].

3. Results

3.1 Spontaneous firing The model presented in this study shows many features observed in whole-cell patch-clamp recording for DA cells in rat midbrain slices. A typical waveform of membrane voltage in spontaneous firing of DA cells of the substantia nigra pars compacta (SNc) is illustrated in Fig. 1A. Membrane voltage of spontaneous firing in the model is shown in Fig. 1B (I_{app}=0 nA/cm^2). It is known that the voltage hyperpolarization immediately after spikes is deeper in DA cells than pyramidal cells in the neocortex; this is represented by the model. In addition, the characteristic slow oscillations were observed in subthreshold membrane voltage after blocking of sodium currents by treatment of DA cells in brain slices with tetrodotoxin (TTX). This observation was also mimicked by reducing the conductance of the voltage-dependent sodium channel in the model (e.g., g_{Na}=0 S/cm^2). The action-potential waveforms from the experiment and the model showed similar spike amplitude and width. Furthermore, the first and second derivatives of the two waveforms also showed similar time courses, which indicated that the model successfully mimicked the shape of action potentials.

3.2 Bifurcation diagram To examine oscillatory phenomena of the model in more detail, a one-parameter (I_{app}) bifurcation diagram was computed (Fig. 2). The oscillation emerges through a supercritical Hopf bifurcation when the externally injected current went beyond a point at I_1. The threshold of the firing cannot be theoretically defined in the supercritical Hopf bifurcation case. However, in this analysis, oscillations where the membrane voltage went beyond +40 mV

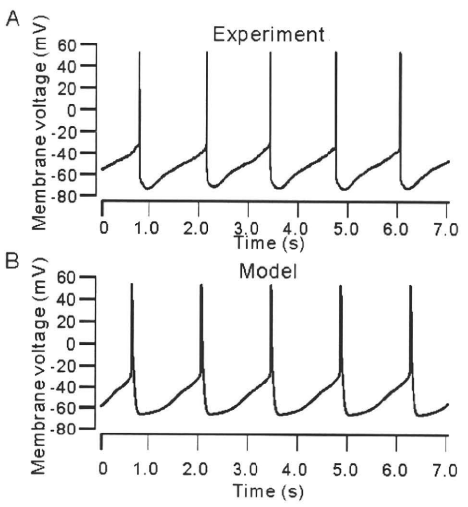

Fig. 1. Comparison of membrane voltage traces. Membrane voltage recorded from a spontaneously active dopaminergic neuron in a rat midbrain slice is shown in A. Membrane voltage of the model can mimic spontaneous firing of rat dopaminergic neurons in whole-cell patch-clamp recording in B.

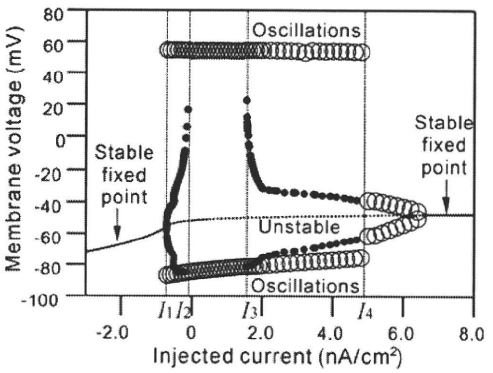

Fig. 2. One-parameter (I_{app}) bifurcation diagram. Solid and dotted lines show stable and unstable fixed points, respectively. Open and filled circles show maximum or minimum voltages in superthreshold and subthreshold oscillations, respectively. The oscillation emerges through a Hopf bifurcation point at I_1 and ends at I=6.51; I_1=−0.716, I_2 =−0.173, I_3=1.56, and I_4=4.69.

were considered as action potentials. In addition to superthreshold oscillations (i.e., action potentials), subthreshold oscillations were observed in two regimes of the intervals [I_1, I_2] and [I_3, I_4]. In the interval between I_2 and I_3, superthreshold oscillations were only observed, and the oscillations corresponded to the spontaneous regular firing shown in Fig. 1B.

3.3 Hyperpolarization-activated current regulates firing frequency In DA neurons in the midbrain, HCN channels are expressed from early postnatal development stages (data not shown here). The HCN channels are activated in hyperpolarized membrane voltage, and the current I_h was actually observed under −70 mV in the voltage-clamp recording. In current-clamp recording, the current component constructs a characteristic membrane-voltage response of so called "sag" (Fig. 3A(a)), and the present model can mimic the voltage response (Fig. 3A(b)). A computational simulation of the model revealed that the conductance (g_h) of HCN channels regulated the firing frequency of spontaneous activity in DA neurons, as illustrated in Fig. 3B. As the conductance increased, the firing rate was monotonically increased until g_h=0.12 and over that value, the rate was decreased. Moreover, the rate was thereafter disrupted discontinuously around g_h=0.15. Over that value, the firing frequency slowed down, because regular firing of action potentials was changed into the mixture of action potentials and subthreshold oscillations. The result indicated that HCN channels regulate not only firing frequency but also the types of oscillations (i.e., regular action potentials or the mixture of sub- and superthreshold oscillations).

3.4 Phase-resetting curves Next, to understand the relationship between the amount of HCN channel expression and phase changes in periodic cycles of regular spiking, phase-resetting curves (PRCs) were investigated. In Fig. 4A, PRCs with four different g_h values are illustrated. If there was no HCN channel expression (i.e., g_h=0), the PRC was monophasic, and there was no delayed phase regions in the curve. In contrast, as the conductance was increased, a delayed phase appeared and PRCs were biphasic (e.g., g_h=0.15). In addition, with increasing conductance, the amplitude in the advanced phase was decreased, and the amplitude in the delayed phase and the portion to the

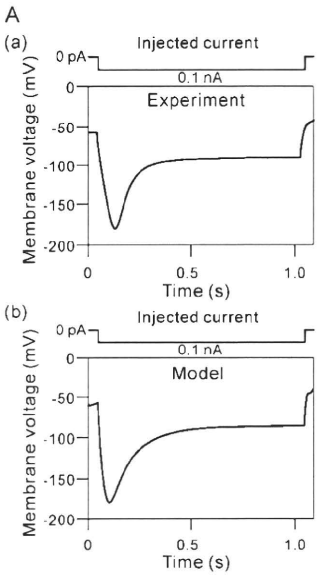

A, Comparison of membrane voltage responses. In response to hyperpolarizing (negative) direct current injection, membrane voltage traces in a representative dopaminergic cell (a) and the present model (b) are shown. The amplitude of the injected current was 0.1 nA in both cases.

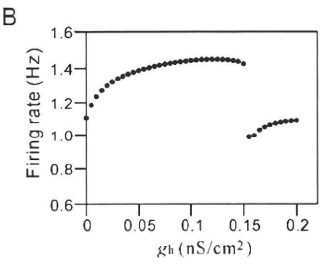

B, A relationship between spontaneous firing frequency and the maximum conductance (g_h) of the HCN channel.

Fig. 3. Electrical properties in the computational model of dopaminergic neurons.

whole phase was increased. In Fig. 4B, the relationships between advanced and delayed phases with g_h are illustrated. The results indicated that the shape of PRCs was regulated by the HCN channel conductance.

3.5 Stability of the coupled phase-equation model

Finally, to understand the relationship between the amount of HCN channel expression and the stability of the model in gap junction-coupled DA neurons, H functions in Eq. (8) and their derivatives were numerically investigated. For four different values of g_h, the H functions and their derivatives are shown in Figs. 5A and B. In all of the H functions, stable fixed points are located at $\phi = 0$ (Fig. 5A), which means that the phase difference $\phi = \theta_1 - \theta_2$ between the two phase-oscillators can eventually converge to zero after a transient period. Therefore, over a transient period, two oscillators are phase-locked and synchronized. However, if there exists a relatively longer time delay τ to the period in the oscillation cycle, a different case happens. This corresponds to a case where, for example, there was

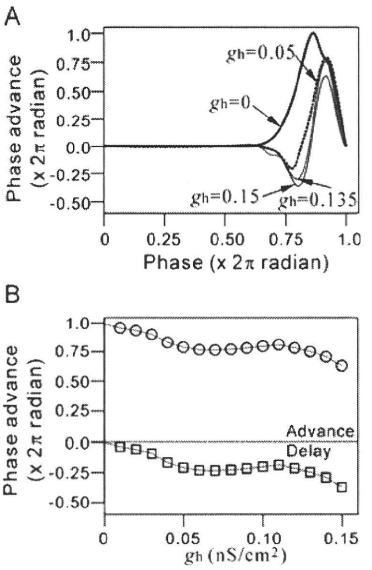

Fig. 4. HCN channel conductance (g_h) dependency in phase resetting curves. Phase resetting curves with four different values of HCN maximum conductance g_h are shown; g_h=0.1, 0.05, 0.135, and 0.15 in A. The curves are normalized by the sum of maximum phase advance and minimum phase delay. The relationships of phase advance (○) and delay (□) vs. g_h are illustrated in B.

a time delay between a spike initiation zone and a gap-junction site. In such a case, each stable fixed point cannot be always located at $\phi = 0$ because of Eq. (9) (Fig. 5B). Moreover, if the time delay is over 10% of the period of unperturbed oscillators, the oscillation can be unstabilized (i.e., $dH(0)/dt<0$ in Fig. 5B). Furthermore, for each ϕ, the area at which $dH(0)/d\phi < 0$ against g_h is shown and illustrated by gray color in Fig. 5C. As explained above, the time delay shifted the gray area downward. In addition, the result shown in Fig. 5C indicated that, as g_h was increased, the region at which $dH(0)/d\phi < 0$ was reduced, so that the time delay τ induced less instability.

In summary, the HCN channel conductance regulated the extent of stability of the coupled oscillators of the model. In addition, if the HCN channels were expressed and the time delay τ was equal to zero or less than 10% of the unperturbed oscillation, the two oscillators were always synchronized and phase-locked.

4. Discussion

DA cells are spontaneously active in both *in vivo* and *in vitro* recordings [1,4]. It is known that adult DA neurons are Ca^{2+}-dependent autonomous pacemakers; that is, their basal activity is intrinsically driven by voltage-dependent L-type Ca^{2+} channels [4]. Voltage-dependent Ca^{2+} channels are multimeric proteins in which the pore-forming α-subunit is the principal determinant of gating and pharmacology. L-type Ca^{2+} channels in brain neurons have one of two α-subunits: $Ca_v1.2$ or $Ca_v1.3$. However, genetic deletion of $Ca_v1.2$ and $Ca_v1.3$ Ca^{2+} channels did not stop pacemaking in DA neurons. In contrast, HCN channels

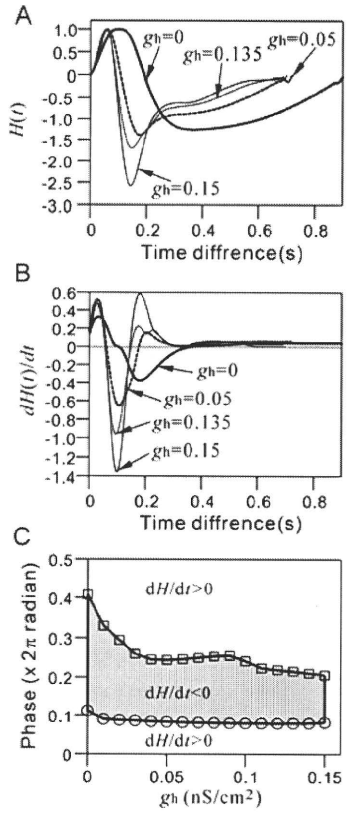

Fig. 5. Stability analysis of the coupled-phase oscillator model. In four different values of g_h (i.e., g_h=0.1, 0.05, 0.135, and 0.15), $H(t)$ functions are shown in A. Here, $t = T_0\phi / (2\pi)$ in the H functions, where T_0 is the period of the uncoupled oscillators. For convenience, $H(t)$ was normalized by the maximum value of each function. Similarly, in the four different values of g_h, the derivatives of $H(t)$ are illustrated in B. Borderlines between positive and negative derivatives of $H(t)$ are illustrated against each g_h in C.

widely partner voltage-dependent Na^+ channels in pacemaking [30]. Recently, Chan et al. reported that, in DA neurons from $Ca_v1.3$ knockout mice, HCN channels were absolutely critical, because an antagonist for these channels completely stopped pacemaking [31]. It is also known that, in DA neurons taken from younger mice (less than three weeks old), HCN channels were also very important in maintaining normal spiking rates [31]. However, as the switch to $Ca_v1.3$-channel–dependent pacemaking evolved, these channels became less important. Therefore, little is known about the functional role of HCN channels in adult DA neurons.

In this study, the conductance-based Hodgkin–Huxley type DA cell model was first constructed on the basis of reported results and data recorded from DA cells in rat midbrain slices. The model mimicked membrane-voltage waveforms in spontaneous firing (Fig. 1B) and responses to hyperpolarizing current injection (Fig. 3Ab). Next, we focused, in particular, on the functional role of HCN channels. As shown in the Results section, if the HCN channel conductance (g_h) was increased, the firing rate was monotonically increased until some value, and over the value, the rate was decreased (Fig. 3B). The result indicated that there can be an optimal value of g_h for maximizing spontaneous firing rate in DA neurons.

Second, we numerically analyzed the stability of oscillations in response to direct current injection and obtained the bifurcation diagram (Fig. 2B). The bifurcation analysis of the model revealed that there was a complex structure for spontaneous firing and for evoked firing even in response to a simple direct current injection. In some parameter ranges, a mixture of action potentials and subthreshold oscillations was observed. A variety in the amount of HCN channel expression could provide more complexity in the bifurcation structure owing to the discontinuity of the relationships between firing rate and HCN channel conductance (Fig. 3B).

Third, to gain some insight into synchronized phenomena in gap junction-coupled DA neurons, a weakly coupled phase-equation model of two identical DA neurons was derived after numerically computing PRCs of regular firing using the conductance-based model. The analysis revealed that the shape of PRCs tightly depended on HCN channel conductance, and a HCN-channel conductance-dependent transition from monophasic to biphasic PRCs was found. The transition was critical for the maintenance of synchronization and phase-locking of the coupled oscillators. In addition, to examine synchronized phenomena among DA cells, a stability analysis of synchronization between coupled oscillators was applied to the model. The results indicated that HCN channels can regulate not only the frequency of firing and subthreshold oscillations in membrane voltage but also the extent of synchronization and desynchronization among DA cells. Thus, in regards to the main autonomous-pacemaking role of adult DA neurons, HCN channels in younger aged animals are similar to L-type Ca^{2+} channels [31]. However, we show here that HCN channels can also contribute to the maintenance of synchronization in coupled oscillations and stability of synchronization regions in gap-junction coupling between DA neurons.

In many neurons of the central nervous system, hormones and neurotransmitters that elevate cyclic adenosine monophosphate (cAMP) levels facilitate activation of I_h by shifting the voltage values for half-maximal activation ($V_{0.5}$) to more positive values and by accelerating the opening kinetics. It has been shown that, in DA neurons, the acceleration of the opening kinetics with cAMP can be attributed to the shift in voltage dependence of activation [32]. Thus, in the presence of high cAMP concentrations, I_h channel opening is faster and more complete than at low cAMP levels. As it is also known that HCN channels are expressed by SNc and VTA DA neurons, they are exquisitely sensitive to allosteric regulation by cAMP [32]. Because SNc DA neurons expressed Ca^{2+}-inhibited isoforms of the enzyme that produces cAMP, it is plausible that rising intracellular Ca^{2+} concentrations dampen cAMP synthesis, leading to a shift in HCN gating in a relatively longer time scale. Hence, the activation of HCN channels can be regulated by the cAMP level and the Ca^{2+} concentration [31].

5. Conclusion

To understand the functional role of HCN channels, we constructed a conductance-based model of DA cells. To test the validity of the model, spontaneous firing and membrane voltage responses evoked by hyperpolarizing current injection were compared with those from actual DA cells of midbrain slices in

in-vitro recordings. The model analysis revealed that HCN channels can regulate not only the frequency of firing and subthreshold oscillations in membrane voltage but also the extent of synchronization and desynchronization among DA cells. Hence, HCN channels not only in premature DA cells but also in adult DA cells have special functional roles in the regulation and maintenance of cooperative firing through gap-junction coupling between DA cells.

Appendix A

A.1 The transient Na^+ current (I_{Na}) is described by

$$I_{Na} = g_{Na} m_{Na}^3 n_{Na} (V - E_{Na}),$$

and the voltage-dependent activation and deactivation functions and time-constant functions are as follows:

$$m_\infty(V) = 1.0 / \left[\exp\left(-(V + 18.0)/7.41\right) + 1.0\right]$$
$$\tau_m(V) = 0.0369 + 0.0791 \exp\left(-(V + 21.2)^2 / 1403.8\right)$$
$$n_\infty(V) = 1.0 / \left[\exp\left((V + 47.8)/3.96\right) + 1.0\right]$$
$$\tau_n(V) = 2.02 + 50.9 \exp\left(-(V + 56.5)^2 / 296.8\right)$$

A.2 The delayed rectifier K^+ current (I_K) is described by

$$I_K = g_K m_K^4 (V - E_K),$$

and the voltage-dependent activation and time-constant functions are as follows:

$$m_\infty(V) = 1.0 / \left[\exp\left(-(V + 34.4)/8.99\right) + 1.0\right]$$
$$\tau_m(V) = 0.201 + 14.4 \exp\left(-(V - 17.2)^2 / 1084\right)$$

A.3 The A-type potassium current (I_A) is described by

$$I_A = g_A m_A^3 n_A (V - E_K),$$

and the voltage-dependent activation and deactivation functions and time-constant functions are as follows:

$$m_\infty(V) = 1.0 / \left[1.0 + \exp\left(-(V + 62.4)/16.0\right)\right]$$
$$\tau_m(V) = 1.62 + 7.99 \exp\left(-(V + 102.2)^2 / 3952\right)$$
$$n_\infty(V) = 1.0 / \left[1.0 + \exp\left(-(V + 83.9)/5.66\right)\right]$$
$$\tau_n = 26.8$$

A.4 The M-type potassium current (I_M) is described by

$$I_M = g_M m_M (V - E_K),$$

and the voltage-dependent activation and time-constant functions are as follows:

$$m_\infty(V) = 1.0 / \left[\exp\left(-(V + 41.5)/5.47\right) + 1.0\right]$$
$$\tau_m(V) = 87.5 + 172 \exp\left(-(V + 25.4)^2 / 735.0\right)$$

A.5 The h-type cation current (I_h) is described by

$$I_h = g_h m_h (V - E_h),$$

and the voltage-dependent activation and time-constant functions are as follows:

$$m_h(V) = 1.0 / \left[1.0 + \exp\left((V + 69.9)/10.5\right)\right]$$
$$\tau_m(V) = 320 + 1850 \exp\left(-(V + 81.0)^2 / 18.1\right).$$

A.6 In the model, four different types of calcium currents are included. The L-type calcium current (I_{CaL}) is described by

$$I_{CaL} = g_{CaL} m_{CaL} (V - E_{Ca}),$$

and the voltage-dependent activation and time-constant functions are as follows:

$$m_\infty(V) = 1.0 / \left[1.0 + \exp\left(-(V + 31.4)/5.34\right)\right]$$
$$\tau_m(V) = 4.7 + 11.7 \exp\left(-(V + 54.2)^2 / 1034\right).$$

The N-type calcium current (I_{CaN}) is described by

$$I_{CaN} = g_{CaN} m_{CaN} n_{CaN} (V - E_{Ca}),$$

and the voltage-dependent activation and time-constant functions are as follows:

$$m_\infty(V) = 1.0 / \left[\exp\left(-(V + 24.4)/5.47\right) + 1.0\right]$$
$$\tau_m(V) = 0.0306 + 18.0 \exp\left(-(V + 34.5)^2 / 720.0\right)$$
$$n_\infty(V) = 1.0 / \left[\exp\left((V + 54.5)/5.34\right) + 1.0\right]$$
$$\tau_n(V) = 49.8 + 450 \exp\left(-(V + 70.5)^2 / 501.4\right)$$

The P-type calcium current (I_{CaP}) is described by

$$I_{CaP} = g_{CaP} m_{CaP} n_{CaP} (V - E_{Ca}),$$

and the voltage-dependent activation and time-constant functions are as follows:

$$m_\infty(V) = 1.0 / \left[\exp\left(-(V + 25.9)/5.38\right) + 1.0\right]$$
$$\tau_m(V) = 0.569 + 10.4 \exp\left(-(V + 38.1)^2 / 765.6\right)$$
$$n_\infty(V) = 1.0 / \left[\exp\left((V + 64.9)/1.87\right) + 1.0\right]$$
$$\tau_n(V) = 14.5 + 389 \exp\left(-(V + 75.5)^2 / 21.5\right)$$

The T-type calcium current (I_{CaT}) is described by

$$I_{CaT} = g_{CaT} m_{CaT} n_{CaT} (V - E_{Ca}),$$

and the voltage-dependent activation and time-constant functions are as follows:

$$m_\infty(V) = 1.0 / \left[\exp\left(-(V + 62.4)/1.19\right) + 1.0\right]$$
$$\tau_m(V) = 12.0 + 65.0 \exp\left(-(V + 68.0)^2 / 36.0\right)$$
$$n_\infty(V) = 1.0 / \left[\exp\left((V + 75.3)/2.77\right) + 1.0\right]$$
$$\tau_n(V) = 10.0 + 50.0 \exp\left(-(V + 72.0)^2 / 100\right)$$

A.7 The Calcium-activated potassium SK current (I_{SK}) is described by

$$I_{SK} = g_{SK}([Ca^{2+}]_i)(V - E_K).$$

Acknowledgements. This work was supported by the Funding Program for Next Generation World-Leading Researchers (NEXT program), Precursory research for Embryonic Science and Technology (PRESTO), Japan Science and Technology Agency (JST) and Grant-in-Aid for Scientific Research (B) and Exploratory Research, the Ministry of

Education, Culture, Sports, Science and Technology (MEXT).

(Manuscript received Jan. 00, 2000, revised May 00, 2000)

References

(1) Schultz W. Getting formal with dopamine and reward. *Neuron* 2002; **36(2)**:241–263.

(2) Brozoski TJ, Brown RM, Rosvold HE, Goldman PS. Cognitive deficit caused by regional depletion of dopamine in prefrontal cortex of rhesus monkey. *Science* 1979; **205(4409)**:929–932.

(3) Graybiel AM, Aosaki T, Flaherty AW, Kimura M. The basal ganglia and adaptive motor control. *Science* 1994; **265(5180)**:1826–1831.

(4) Liss B, Roeper J. Individual dopamine midbrain neurons: functional diversity and flexibility in health and disease. *Brain Research Reviews* 2008; **58(2)**:314–321.

(5) Wahl-Schott C, Biel M. HCN channels: structure, cellular regulation and physiological function. *Cellular and molecular life sciences* 2009; **66(3)**: 470–494.

(6) Tateno T. A small-conductance Ca^{2+}-dependent K^+ current regulates dopamine neuron activity: a combined approach of dynamic current clamping and intracellular imaging of calcium signals. *Neuroreport* 2010; **21(10)**: 667–674.

(7) Hodgkin AL, Huxley AF. A quantitative description of membrane current and its application to conduction and excitation in nerve. *Journal of Physiology* 1952; **117(4)**:500–544.

(8) Amini B, Clark JW, Canavier CC. Calcium dynamics underlying pacemaker-like and burst firing oscillations in midbrain dopaminergic neurons: a computational study. *Journal of Neurophysiology* 1999; **82(5)**: 2249–2261.

(9) Kuznetsov AS, Kopell NJ, Wilson CJ. Transient high-frequency firing in a coupled-oscillator model of the mesencephalic dopaminergic neuron. *Journal of Neurophysiology* 2006; **95(2)**: 932–947.

(10) Yang F, Feng L, Zheng F, Johnson SW, Du J, Shen L, Wu CP, Lu B. GDNF acutely modulates excitability and A-type K^+ channels in midbrain dopaminergic neurons. *Nature Neuroscience* 2001; **4(11)**: 1071–1078.

(11) Koyama S, Appel SB. A-type K^+ current of dopamine and GABA neurons in the ventral tegmental area. *Journal of Neurophysiology* 2006; **96(2)**: 544–554.

(12) Liss B, Roeper J. ATP-sensitive potassium channels in dopaminergic neurons: transducers of mitochondrial dysfunction. *News in physiological sciences* 2001; **16**: 214-217.

(13) Brown DA, Adams PR. Muscarinic suppression of a novel voltage-sensitive K^+ current in a vertebrate neurone. *Nature* 1980; **283(5748)**: 673-676.

(14) Lacey MG, Calabresi P, North RA. Muscarine depolarizes rat substantia nigra zona compacta and ventral tegmental neurons in vitro through M1-like receptors. *Journal of Pharmacology and Experimental Therapeutics* 1990; **253(1)**: 395-400.

(15) Koyama S, Appel SB. Characterization of M-current in ventral tegmental area dopamine neurons. *Journal of Neurophysioogyl* 2006; **96(2)**: 535-543.

(16) Mercuri NB, Bonci A, Calabresi P, Stefani A, Bernardi G. Properties of the hyperpolarization-activated cation current I_h in rat midbrain dopaminergic neurons. *European Journal of Neuroscience* 1995; **7(3)**: 462-469.

(17) Liu Z, Bunney EB, Appel SB, Brodie MS. Serotonin reduces the hyperpolarization-activated current (I_h) in ventral tegmental area dopamine neurons: involvement of 5-HT2 receptors and protein kinase C. *Journal of Neurophysiology* 2003; **90(5)**: 3201-3212.

(18) Durante P, Cardenas CG, Whittaker JA, Kitai ST, Scroggs RS. Low-threshold L-type calcium channels in rat dopamine neurons. *Journal of Neurophysiology* 2004; **91(3)**: 1450-1454.

(19) Kang Y, Kitai ST. Calcium spike underlying rhythmic firing in dopaminergic neurons of the rat substantia nigra. *Neuroscience Research* 1993; **18(3)**: 195-207.

(20) Silva NL, Pechura CM, Barker JL. Postnatal rat nigrostriatal dopaminergic neurons exhibit five types of potassium conductances. *Journal of Neurophysiology* 1990; **64(1)**: 262-272.

(21) Kohler M, Hirschberg B, Bond CT, Kinzie JM, Marrion NV, Maylie J, Adelman JP. Small-conductance, calcium-activated potassium channels from mammalian brain. *Science* 1996; **273(5282)**: 1709-1714.

(22) Wilson CJ, Callaway JC. Coupled oscillator model of the dopaminergic neuron of the substantia nigra. *Journal of Neurophysiology* 2000; **83(5)**: 3084-3100.

(23) Ermentrout B. *Simulating, Analyzing, and Animating Dynamical Systems: A Guide to XPPAUT for Researchers and Students:* Society for Industrial Mathematics Philadelphia; 2002.

(24) Winfree AT. *The Geometry of Biological Time:* Springer: New York; 2001.

(25) Tateno T, Robinson HP. Phase resetting curves and oscillatory stability in interneurons of rat somatosensory cortex. *Biophys J* 2007; **92(2)**: 683-695.

(26) Williams TL, Bowtell G. The calculation of frequency-shift functions for chains of coupled oscillators, with application to a network model of the lamprey locomotor pattern generator. *Journal of Computational Neuroscience* 1997; **4(1)**: 47-55.

(27) Kopell N, Ermentrout GB. Oscillator death in systems of coupled neural oscillators. *SIAM Journal on Applied Mathematics* 1990; **50(1)**: 125-146.

(28) Hoppensteadt FC, Izhikevich EM. *Weakly Connected Neural Networks.* Springer. New York; 1997.

(29) Kopell GB, Ermentrout N. Mechanisms of phase-locking and frequency control in pars of coupled neural oscillators, in *Handbook of Dynamical Systems.* B. Fiedler, ed., Berlin: Elesevier, 2002, pp. 3-54.

(30) Surmeier DJ, Mercer JN, Chan CS. Autonomous pacemakers in the basal ganglia: who needs excitatory synapses anyway? *Curremt Opinion in Neurobiology* 2005; **15(3)**: 312-318.

(31) Chan CS, Guzman JN, Ilijic E, Mercer JN, Rick C, Tkatch T, Meredith GE and Surmeier DJ. 'Rejuvenation' protects neurons in mouse models of Parkinson's disease. *Nature* 2007; **447(7148)**: 1081-1086.

(32) Zolles G, Klocker N, Wenzel D, Weisser-Thomas J, Fleischmann BK, Roeper J, Fakler B. Pacemaking by HCN channels requires interaction with phosphoinositides, *Neuron* 2006;**52(6)**: 1027–1036.

Takashi Tateno (Member) received B.E., M.E., and Ph.D. degrees in Biophysical Engineering from the Osaka University, Japan, in 1992, 1994, and 1999, respectively. In 1994, he joined NTT Basic Research Laboratories, where he was engaged in research in the field of neuroscience. Since 1999, he has been with Osaka University. From 2002 to 2004, he was a visiting researcher at the Department of Physiology, University of Cambridge, U.K. Since 2007, he has been an associate professor of Graduate School of Engineering Science, Osaka University.

論　文

中脳ドーパミン細胞における形態発達の特徴と受動的膜モデルの一構成法

正員　舘野　　高*,**

Morphological Properties in Dopaminergic Neurons of the Rat Midbrain during Early Developmental Stages and One Numerical Approach to Passive-Membrane Modeling

Takashi Tateno*,**, Member

In this study, I aim to understand morphological changes in dopaminergic neurons of the rat midbrain during early developmental stages and their computational properties in the dendrites. To this end, firstly, I measured morphological details of dopaminergic neurons using an immunochemical double-staining technique. In the viewpoint of the Rall's equivalent-cylinder model, secondly, I tested if the data satisfied one of conditions (3/2 power law) of the Rall's model. On the basis of the experimental data, I next investigated if some branches in the individual dendrites had special selectivity in efficient passive propagation of membrane potentials between the branches of individual cells and different cells. The results show that the Rall's 3/2 power law was not satisfied in many branch points and that among branches of each dendrite, specific selectivity in efficient propagation was not found. In addition, I note an implementation method in which the finite element method is applied to one-dimensional cable model of dendrites and give some numerical examples.

キーワード：樹状突起，ドーパミン細胞，有限要素法，免疫化学染色法

Keywords：dendrite, dopaminergic neuron, finite element method, immunochemical staining

1. はじめに

大脳基底核は大脳皮質下核であり，解剖学的には，線条体とその他の複合核（淡蒼球，黒質，視床下核）に大別される。大脳基底核は，体性運動機能に関与し，行動や情動を支配する辺縁系を統合する部位と考えられる[1]。近年，特に，逐次系列の行動障害やパーキンソン病などの運動障害[2]，および，強化学習[3]の関連から，線条体と並んで，黒質の局所回路網とドーパミン作動性細胞が注目されている。

パーキンソン病の特徴である運動症状を引き起こす原因は，黒質緻密部にあるドーパミン作動性（DA）神経細胞数の減少であると考えられている。しかし，何故DA細胞が傷害を受けやすいかは現時点で明らかではないが，細胞内のカルシウム濃度上昇が主要な因子であるとの説がある[4]。近年，Chanらは，DA細胞がCa^{2+}チャネルに依存して律動的活動を維持しており，この依存性が加齢と共に強くなることを示した[5]。また，高血圧や脳卒中の治療に使われるカルシウム拮抗薬のイスラジピンを投与することで，成人の神経細胞を若年の神経細胞と同様に，Na^+/HCNチャネル依存性に逆戻りさせることが可能であることが知られている。特に，パーキンソン病のマウスモデルでは，この「若返り」がDA細胞を保護することから，この方法で病気の進行を遅らせる可能性が示唆されている[5]。さらに，DA細胞は，樹状突起から神経伝達物質ドーパミンを放出し，その効果は抑制性であることから，活動に依存して自己抑制をかける仕組みをもつことが知られている[6]。

上記のような理由から，DA神経細胞のイオンチャンル特性とその細胞形態を含めたダイナミクスを詳細に理解することは，パーキンソン病などの脳疾患にとって重要である。近年，このような背景から，DA神経細胞の数理モデルがいくつか提案されている[7][8]。しかし，その多くは現象論的事実を単純な数式で置き換えたものに過ぎず，実験データに基づいておらず，新たな実験の検証に堪え得るものではない。また，実験で得られた細胞形態データを詳細に再現するモデルも現時点では存在しない。

Rallは1950年代から始まる先駆的な研究によって，樹状突起の電気的特性をモデル化する理論的枠組みを与えた[9]。特に，Rallは枝分かれする樹状突起を受動的膜として膜電位

* 科学技術振興機構　さきがけ
〒332-0012　埼玉県川口市本町4-1-8
PRESTO, JST
4-1-8, Honcho, Kawaguchi, Saitama 332-0012
** 大阪大学大学院　基礎工学研究科
〒560-8531　大阪府豊中市待兼山町1-3
Graduate School of Engineering Science, Osaka University
1-3, Machikaneyama-cho, Toyonaka-shi, Osaka 560-8531

を解析的に扱う線形ケーブル理論[9]と樹状突起を非線形興奮性膜として膜電位を数値的に計算するコンパートメントモデル[10]を脊髄の運動ニューロンに応用した[9][11]。

本研究では，黒質，および，腹側被蓋野のドーパミン細胞の発達に伴う変化を，その特徴と機能の両面から理解することを目指しており，その中で，特に黒質の DA 細胞の形態的特徴を研究の対象としている。本研究では，まず，細胞形態の初期発達を理解するために，二重免疫染色法を用いて，生後 3 日目，および，15 日目の 2 つのステージにおけるラット中脳黒質の DA 細胞の形態を計測した。そして，それらの細胞形態の特徴を定量化した。ラットは生後 10 日前後で聴覚末梢系の細胞が分化し，生後 13 日前後の開眼によって視覚が機能発達を始める。また，この発達ステージで細胞間の電気的シナプスが急激に減少することが知られており[5]，それに伴う神経回路網のダイナミクスの変化の解析は興味深い問題である。次に，Rall のモデル化の観点から神経細胞形態の受動的特性を理解するために，実際に計測した細胞形態データに基づき，DA 細胞が Rall の等価シリンダ (Rall's equivalent cylinder) モデルの条件を満たすか否かを検討した。さらに，有限要素法を応用した樹状突起モデルの一構成法の計算機による実装方法と，その方法の具体的な応用例を述べる。

2. 方　法

〈2·1〉 Rall の等価シリンダモデルと幾何学的比　以下の 2 つの条件が満たされるとき，分岐した樹状突起を 1 本の電気的等価シリンダとして扱うことができることを Rall は示した。(条件 1) 分岐した樹状突起の半径の 3/2 乗の和は分岐前の半径の 3/2 乗に等しい (Rall の 3/2 乗則)。(条件 2) 細胞体から全ての分岐の端までの電気緊張性距離 (electrotonic distance) は等しい。(条件 3) 全ての樹状突起の終端の境界条件は等しい[13]。この条件下で，ある細胞の樹状突起に対して，それを等価変換したモデルを Rall の等価シリンダモデルとよぶ。運動ニューロンでは (条件 1) の Rall の 3/2 乗則はほぼ満たされているが，(条件 2) は満たされておらず，分岐の端までの電気緊張性距離は細胞によって様々であることが知られている[14]。

細胞体からの距離 x における等価シリンダの半径は，樹状突起の分岐点後の半径 r_j を使って，関係式：

$$r_{eq}(x)=\left[\sum_j r_j(x)^{3/2}\right]^{2/3} \quad \cdots\cdots(1)$$

を用いて計算する。また，Rall らは幾何学的比 (geometric ratio, GR) を

$$\mathrm{GR}=\sum_j r_j^{3/2}/r_a^{3/2} \quad \cdots\cdots(2)$$

と定義した[15]。ここで，r_a と r_j は各々電位が伝播する前後の樹状突起の半径を表す。ここでは，r_a が細胞体により近い位置とする。Y 字型の分岐点において，GR≠1 の場合には，インピーダンス不整合が生じる。したがって，膜電位伝播において振幅が減衰するために，伝搬効率が悪い場合 (GR>1) と効率が良い場合 (GR<1) が生じる。

〈2·2〉 スライスの作成と単一細胞記録　全ての実験は大阪大学動物実験委員会の承認を受け，大阪大学動物実験規定に基づき行った。実験には生後 3 日齢，および，生後 15 日齢のラット (Wistar rat, 日本 SLC) を使用した。ラットに吸引麻酔を施した後，素早く脳を取り出した。脳を適当な形に切り出した後に，スライス用ステージに固定し周囲を冷却しながら slicing solution (125 mM NaCl, 2.5 mM KCl, 26 mM $NaHCO_3$, 1.25 mM NaH_2PO, 25 mM Glucose, 4 mM $MgCl_2$, 0.1 mM $CaCl_2$, saturated with 95% O_2 and 5% CO_2) に浸した。その後，ビブラトーム (DTK-3000, D.T.K., Kyoto, Japan) を用いて，300 μm 厚の冠状断面切片を作成した。作成した脳スライスは組織回復のために常温の人工脳髄液 (ACSF; 125 mM NaCl, 2.5 mM KCl, 26 mM $NaHCO_3$, 1.25 mM NaH_2PO, 25 mM Glucose, 4 mM $MgCl_2$, 0.1 mM $CaCl_2$, saturated with 95% O_2 and 5% CO_2) に 1 時間浸した。その後，脳スライスを記録用チャンバーに移動した。そして，36℃の ACSF を 2.0 ml/min で灌流させた。ステージ固定型正立顕微鏡 (BX61WI, Olympus 社) を用いて近赤外微分干渉像の観察を行い，ガラス電極を使って細胞膜を破り，電極内液を細胞中に拡散させた。使用したガラス電極の抵抗は 7.0±1.0 MΩ であった。また，電極内液には，0.2%の biocytin を加えた。

〈2·3〉 免疫組織化学法　ガラス電極内液を細胞に拡散させた後に，脳スライスを 4%パラホルムアルデヒドで一晩固定した。固定した脳スライスをリン酸緩衝生理食塩水で洗浄し，冷凍した際の組織の損傷を防ぐため 15%スクロース溶液で 30 分，30%スクロース溶液で 2 時間脱水した。さらに，30%スクロース溶液に浸した脳スライスを液体窒素にスクリュー瓶ごと 15 秒沈め急速に冷凍した。その後，スライスを解凍し Tris 緩衝生理食塩水 (TBS) で洗浄した。バックグラウンドの染色を減らす為に blocking solution (10%ヤギ正常血清，2%ウシ血清アルブミン) に 1 時間浸した後，一次抗体 (mouse anti-tyrosinehydroxylase monoclonal antibody, Chemicon International) を immersion buffer (10%ヤギ正常血清，2%ウシ血清アルブミン，0.5% Triton X in TBS) 内で一晩インキュベートした。次に，TBS で洗浄し，二次抗体 (Alexa Fluor 488 goat anti-mouse IgG, Invitrogen 社) を加えて 1 時間インキュベートした。Biocytin で標識された細胞を染色するために TBS で洗浄した後に，蛍光標識ストレプトアビジン (Alexa Fluor 594 streptavidin, Invitrogen) を加えて 1 時間インキュベートした。

〈2·4〉 細胞形態情報の数値化　共焦点レーザ走査型顕微鏡 (FV-1000, Olympus 社) を用いて，20 倍の対物レンズで，0.5-1.0 μm 間隔になるように固定脳切片の神経細胞形態の蛍光像を 100 枚程度撮影した。この際に，二重免疫染色法によって染色したチロシン水酸化酵素 (tyrosinehydroxylase) 陽性細胞をドーパミン作動性細胞とし，それ以外の細胞と区別した。また，樹状突起分岐点を詳細に調べるために，40 倍の対物レンズを用いて，0.1 μm

間隔で画像を取り込んだ。その後，画像解析ソフトウエア (Neurolucida, MBF Bioscience) を用いて，細胞形態をトレースした。トレースした点をノードと呼び，そのノード，および，エッジを数値化した。ノード数は，1 画像当たり平均して 2,000 点程度とした。また，数値化したデータを基に，ノードにおいて樹状突起の伸張方向に対する垂直断面積を算出し，断面が円であると仮定した場合の半径を計算した。

〈2･5〉 有限要素法によるケーブル方程式の数値計算

通常，円筒形状セグメントの興奮膜の数理モデルは，ケーブル方程式：

$$p(x)\left(c_{\mathrm{M}}\frac{\partial V(x,t)}{\partial t}+\mathcal{I}(x,t)\right)-\frac{\partial}{\partial x}\left(g_A A(x)\frac{\partial V(x,t)}{\partial x}\right)=0$$

$$x\in(0,L),\quad t>0, \qquad \cdots\cdots(3)$$

および，初期条件と両端 2 つの境界条件から構成される。(3) 式では，円筒形の中心軸に沿った長さを x，時間を t (ms)，断面積を $A(x)$，円周長を $p(x)$ とする。また，セグメントの芯 (コア) のコンダクタンスを g_A (mS/cm)，膜容量を c_M (μF/cm^2) とする。$\mathcal{I}(x,t)$ (μA/cm^2) は，膜を透過するイオンチャネル電流項を表す。セグメントの中心軸に沿ったコア電流は，

$$I(x,t)=-g_A A(x)\frac{\partial V(x,t)}{\partial x} \qquad \cdots\cdots(4)$$

である。本計算における境界条件は，シールドエンドとし，特記しない限り，コア電流は終端点において零であるものとする。Altenberger ら[12]は，有限要素法を 1 次元ケーブル方程式に適用した膜電位の計算手法を提案した。彼らは，文献(12)で提案手法の精度や誤差を詳細に検討している。以下では，Altenberger らが提案した手法に従って，セグメントに沿って節 (ノード) を n+1 点設定し，ノード間の n 個の区間を要素 (エレメント) とよぶ。また，セグメントを長さ L (cm) として，ノード点の位置を $0=x_0<x_1<\cdots<x_n$ とする。(3) 式中の関数 $V, \mathcal{I}, p, A$ を三角形形状 (テント) 関数を基底関数として，区間 $x\in[0,L]$ において，

$$V(x,t)=\sum_{k=0}^{n}V_k(t)\phi_k(x),\quad A(x,t)=\sum_{k=0}^{n}A_k\phi_k(x),$$

$$\mathcal{I}(x,t)=\sum_{k=0}^{n}\mathcal{I}_k(t)\phi_k(x),\quad P(x,t)=\sum_{k=0}^{n}P_k\phi_k(x), \qquad \cdots\cdots(5)$$

と展開する。したがって，全区間内の任意点 x の電位 $V(x,t)$ を知るためには，電位のサンプル点の有限要素によって，適当に表現する形式を得ればよい。一般に，基底関数列 $\phi_j(x)$ を用いて，関数 $f(x)$ を展開した場合に，真の関数と近似関数との二乗誤差の全区間に渡る積分値：

$$E(f_0,f_1,\ldots,f_n)=\int_0^L\left[f(x)-\sum_{j=0}^{n}f_j\phi_j(x)\right]^2dx \qquad \cdots\cdots(6)$$

を最小とする係数列 $\{f_j\}_{j=0,\ldots,n}$ を求めることができれば，最小 2 乗誤差の意味で，$f(x)$ の最適な近似関数を得ることができる。実際に，これを実行すれば，(3)式は，

$$P\frac{d\bar{V}}{dt}+P\bar{\mathcal{I}}(t)=A\bar{V} \qquad \cdots\cdots(7)$$

と表記することができる[12]。ただし，ノード点 x_k での電位，断面積，円周長を各々 v_k，a_k，p_k とし，$\Delta x_k=x_k-x_{k-1}$，$\Delta v_k=v_k-v_{k-1}$，および，$a^k=(a_{k-1}+a_k)/2$ とおくと，行列 P は，対角成分要素を次のベクトル：

$$e_1=\quad c_M[\Delta x_1(3p_0+p_1),\ \Delta x_1(3p_0+p_1)+\Delta x_2(p_1+3p_2),\ldots,$$
$$\Delta x_{n-1}(3p_{n-2}+p_{n-1})+\Delta x_n(p_{n-1}+3p_n),\Delta x_n(p_{n-1}+3p_n)]/12$$

の要素として，その上下の対角成分要素を，共に，

$$e_2=c_M\left[\Delta x_1(p_0+p_1),\ldots,\Delta x_n(p_{n-1}+p_n)\right]/12$$

の要素とする行列である。また，同様に，行列 A は，対角成分要素を次のベクトル：

$$u_1=-g_A[a^1/\Delta x_1,a^1/\Delta x_1+a^2/\Delta x_2,\ \ldots,$$
$$a^{n-1}/\Delta x_{n-1}+a^n/\Delta x_n,a^n/\Delta x_n]$$

の要素として，その上下の対角成分の要素を，共に

$$u_2=g_A\left[a^1/\Delta x_1,\ldots,a^n/\Delta x_n\right]$$

の要素とする。また，$\bar{V}$ はノードにおける電位ベクトルを表し，$\bar{V}=[V(x_0,t),\ldots,V(x_n,t)]'$ である。$\bar{\mathcal{I}}(t)$ は，イオンチャネル電流項を表し，受動的な膜の場合は，リーク電流項のみとなる。本研究では，Altenberger ら[12]の分岐構造を持たない有限要素法表現を拡張した。そして，Y 字形状の分岐構造のある樹状突起の膜電位を計算する方法を新たに導出し，その方法を以下では適用した。ここでは詳細は省略するが，その結果から，分岐構造を持たない場合と同様の行列 P_Y, A_Y が得られる。ただし，Altenberger らが用いた単純なシリンダ形状の行列 P, A とは異なり，対角成分とその上下の成分以外にも零でない要素をもつために，計算には注意が必要である。また，(3)式の偏微分方程式とは異なり，(7)式は常微分方程式であり，時間に関する数値計算手法は一般的な Crank-Nicholson 法を用いた。

3. 結　果

〈3･1〉 ドーパミン作動性細胞形態の特徴　Fig. 1A に生後 15 日目の DA 作動性神経細胞の形態を示す。冠状断面の脳切片を作成した為に，線条体等に投射する体軸吻側方向に伸張する軸索は切断されており，Fig. 1A は，主に細胞体と樹状突起であると考えられる。

生後 15 日齢の 11 DA 細胞に対して，(i) 細胞体に接続している主要な樹状突起数は N_d=5.45±1.72 (平均±標準偏差)，(ii) 各樹状突起の分枝に含まれる分岐点数，B=2.81±3.07，(iii) 分岐点間のセグメント内における細胞体からの 1 μm 当たりの各樹状突起半径の減衰率，D=2.05±1.34 %であった。一方，生後 3 日齢の 9 DA 細胞に対して，同様に，(i) N_d=4.83±0.87，(ii) B=5.17±2.10，(iii) D=2.36±1.52%であった。

〈3･2〉 Rall の等価シリンダモデル　Fig. 1B は，Fig. 1A と同じ細胞の樹状突起の樹形図を表している。実験によっ

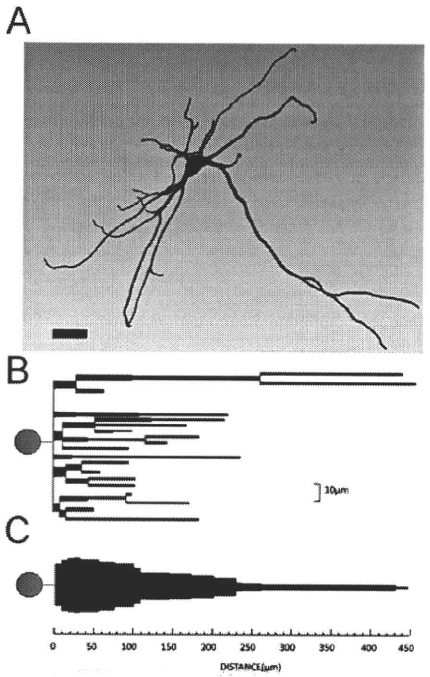

Fig. 1. A, morphology of a dopaminergic neuron from a postnatal day 15 rat. B, schematical representation of dendrites for the cell show in A. C, Rall's equivalent-cylinder representation corresponding one shown in B. A small bar in A indicates 50 μm. Two circles on the left in B and C represent somata.

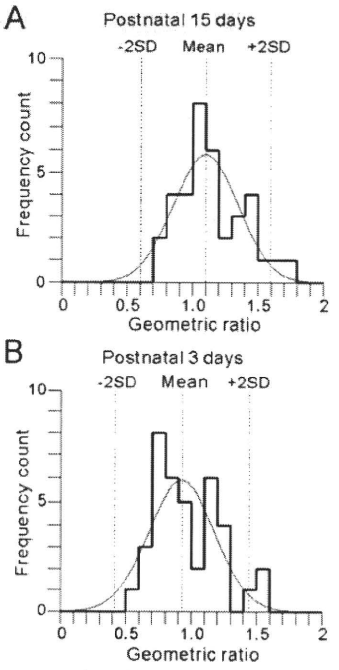

Fig. 2. Histograms for geometric ratio (GR) between a parent branch and daughter branches in dendrites of dopaminergic neurons. A, postnatal 15-day cells. B, postnatal 3-day cells. Dotted lines represent mean and mean ±2SD, respectively. Each curve in the plots shows a normal distribution with the mean and SD.

て得た結果から，(1)式を用いて分岐する樹状突起の半径を等価シリンダモデルに統合させた場合に，この細胞では，前方 1/3 程度が円柱状であり，その後は円錐状の先細り形状になる。Fig. 1C は，その等価ケーブルモデルを表している。Fig. 1C の左端は細胞体を表す。他の DA 細胞でも同様な形状のシリンダとなった。以下では，DA 細胞の形態が単純な Rall の等価シリンダモデルで表現可能であるかを検証する。ここでは，特に，研究方法で述べた（条件 1）を検証する。

〈3·3〉 樹状突起における Rall の幾何学的比 生後 15 日目の 7 細胞 36 箇所の分岐点における GR の分布を Fig. 2A に示す。GR の平均は m=1.010 であり（Fig. 2A 中の点線中央），その標準偏差はσ =0.249 であった。分岐点で Rall の 3/2 乗則が満たされる場合には GR=1 となるために，実際の DA 細胞の多くの分岐点では 3/2 乗則は満たされていない。したがって，(条件 1) が成立しないので，DA 細胞の樹状突起を Rall の等価シリンダで表現して，電気的特性を解析する合理的理由は存在しない。今回の実験で計測したドーパミン細胞の 36 箇所の分岐点では，GR>1 となる分岐点が 23 箇所あり，残りの 13 箇所が GR<1 であった。この結果から，受動的な膜として細胞体から電位が伝播 (backward propagation) する際には，DA 細胞の分岐点での形状は，その数の 60%程度が効率的に伝播しないことが判った。

しかし，反対に，樹状突起末端からシナプス電位が伝播 (forward propagation) する場合には効率が良いことになる。また，細胞間での GR の大きさは，GR=1 を境界として，必ずしも対称に分布しておらず，細胞内でも効率的膜電位伝播となる分岐点とそうではない分岐点が混在することが判った。また，同一細胞の樹状突起の枝においても，GR の値は必ずしも一様ではなかった。

同様に，生後 3 日齢のラットの 10 DA 細胞の 38 箇所の分岐点における GR の分布を Fig. 2B に示す。GR の平均は m=0.926 であり（Fig. 2B の点線中央），その標準偏差は σ =0.257 であった。10 細胞中の 38 箇所の分岐点で，GR>1 が 15 箇所あり，残りの 23 箇所が GR<1 であった。また，細胞間に大きな偏りは見られなかった。さらに，生後 3 日目と 15 日目の GR 分布の歪度 s は，各々s =0.601 と s =0.510 であり，成長後は GR=1 を中心にして，GR の分布の左右の偏りが小さくなることが判る。

〈3·4〉 受動的膜モデルシミュレーション 以降では，生後 15 日齢のラットの DA 細胞の平均的な特徴（分岐数 4，半径の低減率 2.0%）を有する Fig. 3A に概略を示す比較的単純な形状の樹状突起モデルを考える。研究方法で述べた電位の数値計算手法を用いて，Fig. 3B では，Rall の GR 値を分岐点で一定値（GR=0.5, 1.0, および，2.0）に固定し，左端の電位を 40 mV に保持した場合について，定常状態での膜電位を位置の関数として表示している。まず，GR=1 の条件下では，分岐点での膜電位が滑らかに変化する。

一方，GR=0.5，あるいは，GR=2.0 の条件では，分岐点で